Since January 2020 Elsevier has created a COVID-19 resource centre with free information in English and Mandarin on the novel coronavirus COVID-19. The COVID-19 resource centre is hosted on Elsevier Connect, the company's public news and information website.

Bioelectrochemistry 137 (2021) 107671

Contents lists available at ScienceDirect

Bioelectrochemistry

journal homepage: www.elsevier.com/locate/bioelechem

An advanced molecularly imprinted electrochemical sensor for the highly sensitive and selective detection and determination of Human IgG

A. Axin Liang, B. Huipeng Hou, C. Shanshan Tang, D. Liquan Sun, E. Aiqin Luo *

Key Laboratory of Molecular Medicine and Biotherapy, School of Life Science, Beijing Institute of Technology, Zhongguancun South Street No.5, 100081, China

ARTICLE INFO

Article history:
Received 31 August 2020
Received in revised form 5 September 2020
Accepted 5 September 2020
Available online 9 September 2020

Keywords:
Human IgG
Molecularly imprinted electrochemical sensor
MoS_2
N-GQDs

ABSTRACT

An advanced molecularly imprinted electrochemical sensor with high sensitivity and selectivity for the detection of Human immunoglobulin G (IgG) was successfully constructed. With acrylamide imprinting systems, surface imprinting on the nanoparticles $CuFe_2O_4$ targeted at IgG was employed to prepare molecularly imprinted polymer, which served as recognition element for the electrochemical sensor. Furthermore, the sensor harnessed a molybdenum disulfide (MoS_2)@nitrogen doped graphene quantum dots (N-GQDs) with ionic liquid (IL) nanocomposite for signal amplification. Under optimized experimental conditions, the sensor shortened the response time to less than 8 min, and the response was linear at the IgG concentration of 0.1–50 ng·mL^{-1} with a low detection limit of 0.02 ng·mL^{-1} (S/N = 3). Our findings suggested that, the sensor exhibited high detectability and long-time stability. The satisfactory results of human serum sample analysis showed that the developed IgG sensor had promising potential clinical applications in detecting IgG content.

1. Introduction

Human immunoglobulin G (IgG) has been identified as the human body antibody with the highest abundance [1–3]. Besides, IgG is the only human immunoglobulin that can pass through the placenta, which exerts a vital part in the anti-infective immunity in newborns [4–6]. IgG is highly expressed in serum and accounts for 75–80% of all immunoglobulins in serum. Typically, it is widely distributed and easily penetrates the capillary wall. Moreover, it is also an important antibody existing outside the blood vessels [7]. The abnormal IgG level will induce certain disorders, like hyperthyroidism and systemic lupus erythematosus (SLE). COVID-19 pandemic outbreak is one of the most shocking scenes of the XXI century. A convenient way to detect the presence of the novel coronavirus is to use substrates (i.e. sensor material) that has been functionalized with recombinant viral antigens and can be used to bind to IgG because these antibodies remain in the blood longer [8]. IgG antibodies are produces during the onset of the infectious disease (around 2 weeks). Therefore, it is of critical importance to detect the content of IgG in the fields of quality monitoring, drug research and medical diagnosis [9,10].

To date, various analytical techniques such as radial immunodiffusion, enzyme-linked immunoassays, immune nephelometry and fluorescent immunoassays, have been proposed in literature for the determination of IgG [11–15]. However, most of these techniques have some limitations such as expensive and cumbersome instruments, complicated pretreatment step, and time consuming analysis. Compared with these instrumental methods, the electrochemical measurement of IgG has the advantage of simplicity, high sensitivity, fast response and low detection limit [16,17]. Extensive efforts have been made to electrochemically determine immunoglobulins, notably, the isotype of IgG which is dominant during low content detection in a majority of studies [18,19].

Currently, many studies have depicted numerous diverse strategies in preparing the IgG-specific electrochemical sensors that can be used as the classic model analyte [20–22]. Generally, the electrochemical sensors based on nanomaterials can enhance sensor sensitivities through boosting the transducer electrochemical performances and using the biorecognition molecules to increase the sensing surface loading [23–26]. Glassy carbon electrode (GCE) is the basis of a majority of electrochemical sensors, and conductive nanomaterials are then used to modify GCE for improving its sensitivity to target analytes [27,28]. Many novel nanomaterials can be applied in modifying GCE, including MoS_2 [29,30], metal nanoparticles [31,32], graphene quantum dot [33] and carbon black [34,35].

MoS_2 is a typical dichalcogenide, which attracts wide interests in numerous fields, such as hydrogen catalysis and storage, capacitors, and electrochemical device [36,37]. However, because the

* Corresponding author.
E-mail address: bitluo@bit.edu.cn (E. Aiqin Luo).

https://doi.org/10.1016/j.bioelechem.2020.107671
1567-5394/

conductivity of MoS_2 is still lower than that of carbon-based materials, little attention has been paid to the application of MoS_2 as an electrode material for sensors [38]. Therefore, it is suggested to combine MoS_2 with carbon-based materials to show a synergistic effect on the application of electrocatalysis [39]. Guochuang Huang et al. obtained a layered MoS_2-Graphene composite modified electrode with good electrochemical performance, and it was able to detect paracetamol with high sensitivity and selectivity by L-cysteine assisted liquid phase method [40]. Tong Guo et al. designed a novel three-dimensional (3D) layered MoS_2@graphene functionalized with N-GQDs composites, which was used as an enhanced electrochemical hydrogen evolution catalyst [41]. As a result, it is reasonable to speculate that, integrating the layer-structured MoS_2 with nitrogen-doped graphene quantum dots (N-GQDs) also exerts same function in electrochemical sensors and electrocatalysis.

Moreover, more and more importance has been attached to ionic liquids (IL) during sensor construction due to optimized structures and properties, distinguishable anion/cation combination, high conductivity, remarkable biocompatibility, and good thermostability [42,43]. Ionic liquid is an effective modifier to improve the sensing performance of electrode [44]. These results indicate that the use of ionic liquids can improve reaction sensitivity and promote efficient direct electron transfer of various redox biomolecules. Therefore, based on the strong electrostatic-chemical interaction between IL and MoS_2@N-GQDs and the improvement dispersion by IL, the addition of IL is expected to further enhance the electrochemical signal in the fabrication of sensor.

The recognition element is a vital part in electrochemical sensor. Numerous recognition elements are adopted for improving electrochemical sensor selectivity and sensitivity, such as aptamers, phages, antibodies, as well as the molecularly imprinted polymers (MIPs) [45–48]. Molecular imprinting has been developed as a typical recognition site formation process induced by the template within the polymer [49]. Those molecularly imprinted synthetic receptors have exhibited integrated properties, including high affinity, robustness, low production cost, and great specificity. As a result, they may serve as the promising candidate natural receptors [50–52]. Great advances have been attained in the fields of nanotechnology and polymer science, which have strengthened the performances of molecularly imprinted polymer (MIP) sensors. Many high-quality articles have been published recently to describe MIP sensors in determining explosives, abused drug and biomolecules, which facilitate applying such technique in the forensic and medical diagnostic fields [53–55]. Specifically, the magnetic $CuFe_2O_4$ nanoparticles (NPs) have been used as the carriers of the surface-imprinted modified electrochemical sensors, which is ascribed to their superparamagnetism, high specific capacitance, favorable biocompatibility and excellent electroconductibility. Our research group prepared a novel electrochemical sensor based on the MIPs modified $CuFe_2O_4$ glassy carbon electrode (GCE) to electrochemically detect lysozyme [56].

This study aimed to develop an electrochemical sensor to selectively detect IgG. The methods used were shown below (Schematic 1). Firstly, the MoS_2@N-GQDs-IL nanocomposite with high conductivity was used to modify the GCE, so as to amplify the electrochemical signal. Molybdenum disulfide (MoS_2) served as the skeleton with electric conduction, and functionalized with nitrogen doped graphene quantum dots (N-GQDs) in which MoS_2 and N-GQDs exist in a bonding manner of Mo-N. Based on the strong electrostatic chemical interactions between ionic liquid and MoS_2@N-GQDs and the improvement of dispersion of MoS_2@N-GQDs by ionic liquid, the combination of ionic liquid and MoS_2@N-GQDs provides an effective platform for sensitive electrochemical sensing. Secondly, IgG was used as the template, while $CuFe_2O_4$ was utilized as the carrier to prepare the surface-imprinted $CuFe_2O_4$ MIPs NPs, which were used as recognition elements for the electrochemical sensor. Thereafter, cyclic voltammetry (CV) and differential pulse voltammetry (DPV) were applied to assess the electrochemical response of the MIPs NPs/MoS_2@N-GQDs-IL/GCE electrode to IgG quantification. Specifically, this study focused on examining the stability, selectivity, accuracy and reproducibility for our as-prepared MIPs NPs/MoS_2@N-GQDs-IL/GCE electrode, as well as the feasibility of our developed sensor in detecting IgG in whole blood samples.

2. Experiment procedures

2.1. Chemicals

Human serum immunoglobulin G (IgG) was obtained from Sigma-Aldrich (St. Louis, MO, USA), which was utilized as received with no additional purification. Lysozyme (Lyz) and bovine serum albumin (BSA) were purchased from Solarbio stock. Albumin from human serum (HSA) was provided by Shanghai yuanye Bio-Technology Co., Ltd (Shanghai, China). Iron (III) chloride hexahydrate ($FeCl_3{\cdot}6H_2O$), potassium ferricyanide [$K_3Fe(CN)_6$], sodium acetate (NaAc), copper (II) chloride dihydrate ($CuCl_2{\cdot}2H_2O$), and potassium chloride (KCl) were provided by Beijing Tong Guang Fine Chemicals (Beijing, China). 1-Benzyl-3-methylimidazolium tetrafluoroborate ([BzMlm]BF_4) was ordered by Lanzhou Insititute of Chemical Physics (Lanzhou, China). N,N,N',N'-Tetramethylethylenediamine (TEMED), dicyandiamide (DCD), L-cysteine and sodium molybdate dihydrate ($Na_2MoO_4{\cdot}2H_2O$) were provided by Sinopharm Chemical Reagent Co., Ltd (Shanghai, China). N,N'-methylene-dipropylene amide (MBA), methacrylic acid (MAA) and acrylic amide (AAm) were provided by Tianjin Fine Chemical Research Institute (Tianjin, China). Poly(n-isopropylacrylamide) (NIPAAm) was provided by Across Organics in Belgium. Polyethylene glycol (PEG 20000) was provided by Xi Long Chemical Co., Ltd (Guangxi, China). Citric acid (CA), trisodium citrate, acetic acid (AA), poly(ethylene glycol), acetonitrile (ACN), hydrochloric acid (HCl) and ammonium persulfate (APS) were provided by Beijing Chemical Works (Beijing, China).

All reagents and solvents adopted in this experiment were analytically pure, which were utilized as received. Each aqueous solution was prepared with ultra-pure water (18.2 MΩ cm). A pH meter (Sartorius PB-10) was used to determine the solution pH.

2.2. Device

CHI6043E electrochemical workstation (CH Instruments, Shanghai, China) was adopted for all electrochemical test, where the traditional three-electrode system was employed consisting of a modified GCE (diameter, 3.0 mm) working electrode, a platinum wire counter electrode, and an AgCl (3 mol·L^{-1} KCl) reference electrode. Shapes and sizes of MoS_2@N-GQDs-IL nanocomposites were determined by the high-resolution H7700 transmission electron microscopy (TEM, Hitachi, Japan) at 100 kV of accelerating voltage using the Tecnai F20G2 (FEI, Netherlands). Scanning electron microscopy (SEM) was conducted using the Inspect F50 microscope (FEI, Netherlands). Afterwards, the Ultima IV X-ray diffractometer (Rigaku, Japan) in the presence of Cu Kα radiation (λ = 1.54178 Å) was applied for X-ray diffraction (XRD). The UV-1800 (Shimadzu, Japan) was adopted to obtain the ultraviolet-visible (UV–vis) spectra. Serum IgG was detected by the BN II automatic protein analyzer (SIEMENS, German).

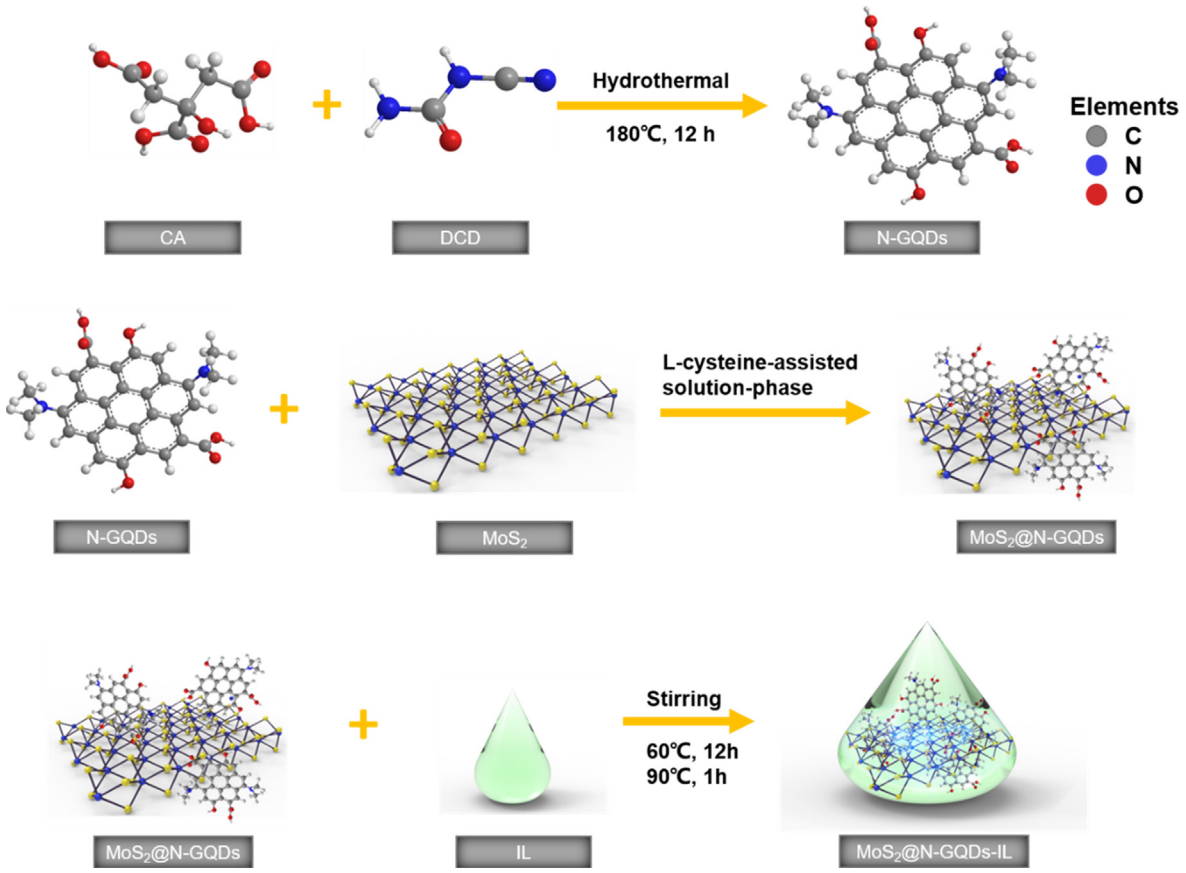

Schematic 1. Synthesis reaction of MoS_2@N-GQDs-IL.

2.3. Solutions

The 2 mg·mL^{-1} stock solutions of HSA, BSA and Lyz were prepared through dissolution into ultra-pure water and the phosphate buffer solution (PBS), and then preserved at +4 °C within the refrigerator. The PBS (pH = 7.4) containing 5 mmol·L^{-1} $K_3Fe(CN)_6$ and 0.1 mol·L^{-1} KCl was adopted for measuring EIS and DPV.

2.4. MoS_2@N-GQDs preparation

The present study prepared N-GQDs through hydrothermal treatment with dicyandiamide and citric acid (CA) as reported in Refs. [57–59]. Briefly, 1 g DCD and 2 g CA were added into 5 mL ultra-pure water during the typical synthetic process, followed by transfer to Teflon lined autoclave (25 mL), 12 h of heating under the temperature of 180 °C, and natural cooling of the reactor to ambient temperature. Then, the ethanol was added into the product, centrifuged at 5000 r/min for 5 min, washed for 3 times, and dried for 24 h within the vacuum drying oven under the temperature of 60 °C to obtain the solid with good water solubility.

The modified solution-phase approach assisted by L-cystein was adopted to prepare MoS_2@N-GQDs composites, and the final optimal composition of N-GQDs and MoS_2 was obtained mainly by references and later experimental optimization [38,60]. Specifically, ultra-pure water (50 mL) was added into the 200 mL beaker, followed by transfer of 0.1 g N-GQDs and addition of Na_2MoO_4 $2H_2O$ (0.5 g) in it. Following 30 min of stirring and ultrasonication, the solution pH was adjusted to 6.5 with the 0.1 mol·L^{-1} HCl. Later, L-cysteine (1.0 g), together with the mixture, was dissolved into ultra-pure water (100 mL), and the resultant mixture was then transferred to the Teflon-lined stainless steel autoclave (100 mL) and tightly sealed, followed by 36 h heating under the temperature of 180 °C. Later, that autoclave was naturally cooled, centrifuged to collect black precipitates, rinsed by ethanol and ultra-pure water, and dried for 24 h at 60 °C within the vacuum oven.

2.5. MoS_2@N-GQDs-IL preparation

MoS_2@N-GQDs-IL composites were prepared according to the published literature, and the final optimal composition of each component was obtained mainly by references and later optimization [61]. To be specific, 0.04 g $[BzMlm]BF_4$ was put to 20 mL of 0.01 g mL^{-1} MoS_2 ultra-pure water dispersion at first, and then stirred continuously for 12 h under the temperature of 60 °C. Thereafter, the as-obtained suspension was put to the oil bath at 90 °C for 1 h. The 0.22 μM filter membrane was used to filter the resultant dispersion solution, followed by 12 h of drying at 60 °C within the vacuum oven (Schematic 1).

2.6. MIPs NPs preparation

The $CuFe_2O_4$ NPs were synthesized according to the hydrothermal approach [56,62]. In brief, 0.408 g $CuCl_2{\cdot}2H_2O$ (2.4 mmol) and 1.296 g $FeCl_3{\cdot}6H_2O$ (4.8 mmol) were immersed into 60 mL ethylene glycol for forming the clear solution. Thereafter, 1 g polyethylene glycol (M = 20,000) and 3.6 g NaAc were slowly added to the as-prepared solution for 1 h, and vigorously stirred under ambient temperature for 24 h to achieve fully dissolved. Then, the as-prepared mixture was transferred to the Teflon-lined stainless steel autoclave (80 mL), heated for 10 h at 200 °C, and then the autoclave was cooled naturally to ambient temperature. Later, the permanent magnet was used to separate those nanohybrid

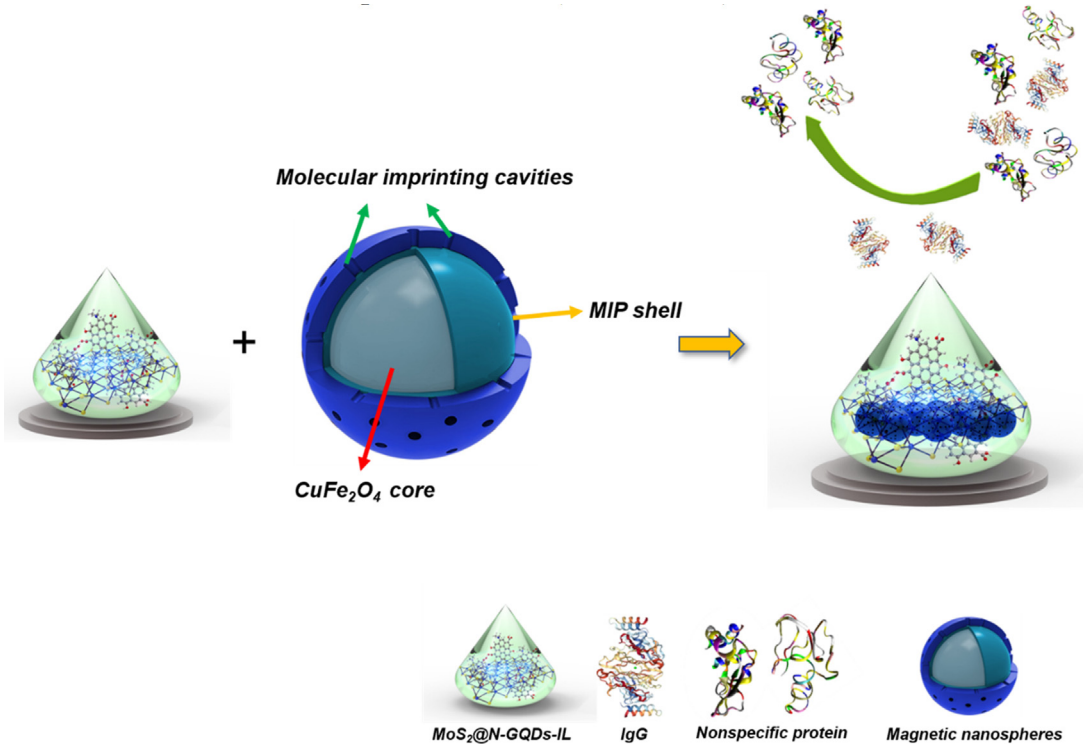

Schematic 2. Electrochemical determination of human IgG using $CuFe_2O_4$ nanoparticles molecularly imprinted polymers modified with MoS_2@N-GQDs-IL.

magnetic materials, which were subsequently centrifuged at 4000 rpm, washed with ethanol and ultra-pure water for 3–5 times, and dried for 5 h using the vacuum freeze drier.

Magnetic MIPs NPs was prepared in the following steps: first of all, 1.4 mmol IgG was dissolved into 0.02 mol·L^{-1} phosphate buffer solution (PBS) (20 mL, pH = 7.4); then, 30 μL MAA, 100 mg NIPAAm, as well as 30 mg AAM were added in succession. Afterwards, the pre-assembled solution was synthesized through 1 h of stirring. 100 mg $CuFe_2O_4$ magnetite was added into 0.02 mol·L^{-1} PBS (20 mL, pH = 7.4) to stir for 20 min. Later, 25 mg N,N'-methy lene-dipropylene amide (MBA) was added into the $CuFe_2O_4$-PBS mixture, and the resultant mixture was then put into the pre-assembled solution. Typically, the mixture was subjected to 1 h of stirring to prepare the pre-polymerized solution, followed by preservation within the three-necked flask. Then, the 30% TEMED (100 μL), together with the 10% wt ammonium persulfate (APS, 20 μL), was put into the polymerization radical initiator for 24 h of reaction at nitrogen atmosphere. Later, magnet separation, and repeated washing with ultra-pure water and ethanol were conducted. Afterwards, the mixture of acetic acid (AA) (10%, v: v) and acetonitrile (ACN) (90%, v: v) was used to wash the MIPs NPs, and template protein was extracted until there was no eluent absorbance at the wavelength of 340 nm.

NIPs NPs were prepared using the same procedure without adding IgG [17,29,57].

2.7. Sensor fabrication

The MoS_2@N-GQDs-IL solution (2 mg/mL) was prepared by dissolving MoS_2@N-GQDs-IL in ultra-pure water. Then, MoS_2@N-GQDs-IL solution (80 μL) was dispersed into MIPs NPs suspension (1 mL) under 30 min of ultrasonication. Before preparation, the alumina slurries (0.05 μm) were used to polish the GCE, followed by sequential ultrasonic cleaning in acetone and ethanol. Later, appropriate MIPs NPs suspension was dripped onto the GCE surface, and the solvent was then evaporated to obtain the imprinted GCE. Non-imprinted MoS_2@N-GQDs-IL/GCE was prepared according to the same procedure except using NIPs NPs instead of MIPs NPs and referred to as the non-imprinted sensor (Schematic 2).

2.8. Electrochemical examinations

Electrochemical measurements were performed in PBS (pH = 7.4) containing 5 mmol·L^{-1} $K_3Fe(CN)_6$ and 0.1 mol·L^{-1} KCl. The volume of solution used was 50 mL. In addition, differential pulse voltammetry (DPV) was measured at a scan potential of −0.2 V to + 0.6 V, a pulse amplitude of 50 mV, a pulse width of 0.05 s, and a scan rate of 100 mV/s. In cyclic voltammetry (CV) mode, scan range was from −0.2 V to + 0.6 V and scan rate was 100 mV/s. Thereafter, the electrochemical impedance spectroscopy (EIS) analysis was recorded at an amplitude of 0.005 V, a potential of 0.24 V, and a frequency range of 0.01–100 kHz.

3. Results and discussion

3.1. MoS_2@N-GQDs-IL characterizations

Fig. 1a presents the SEM images for the resultant MoS_2@N-GQDs-IL, which shows the 3D ball-like structure. Typically, such a 3D structure increased the contact area with analytes. N-GQDs coalescing or overlapping contributed to forming the interlinked conduction network, which also facilitated the quick electron transport during the electrode reaction. As observed from the N-GQDs TEM images in Fig. 1b, the as-prepared N-GQDs were the small sheets that had narrow distribution of size. N-GQDs had the average diameter of 3.75 nm, which was verified by analyzing the images of 100 individual particles. In comparison with those previously reported GQDs (0.5–2 nm in thickness and 15 nm in diameter) [63], the N-GQDs prepared in this study exhibited much lower lateral size while similar height. The representative MoS_2-IL

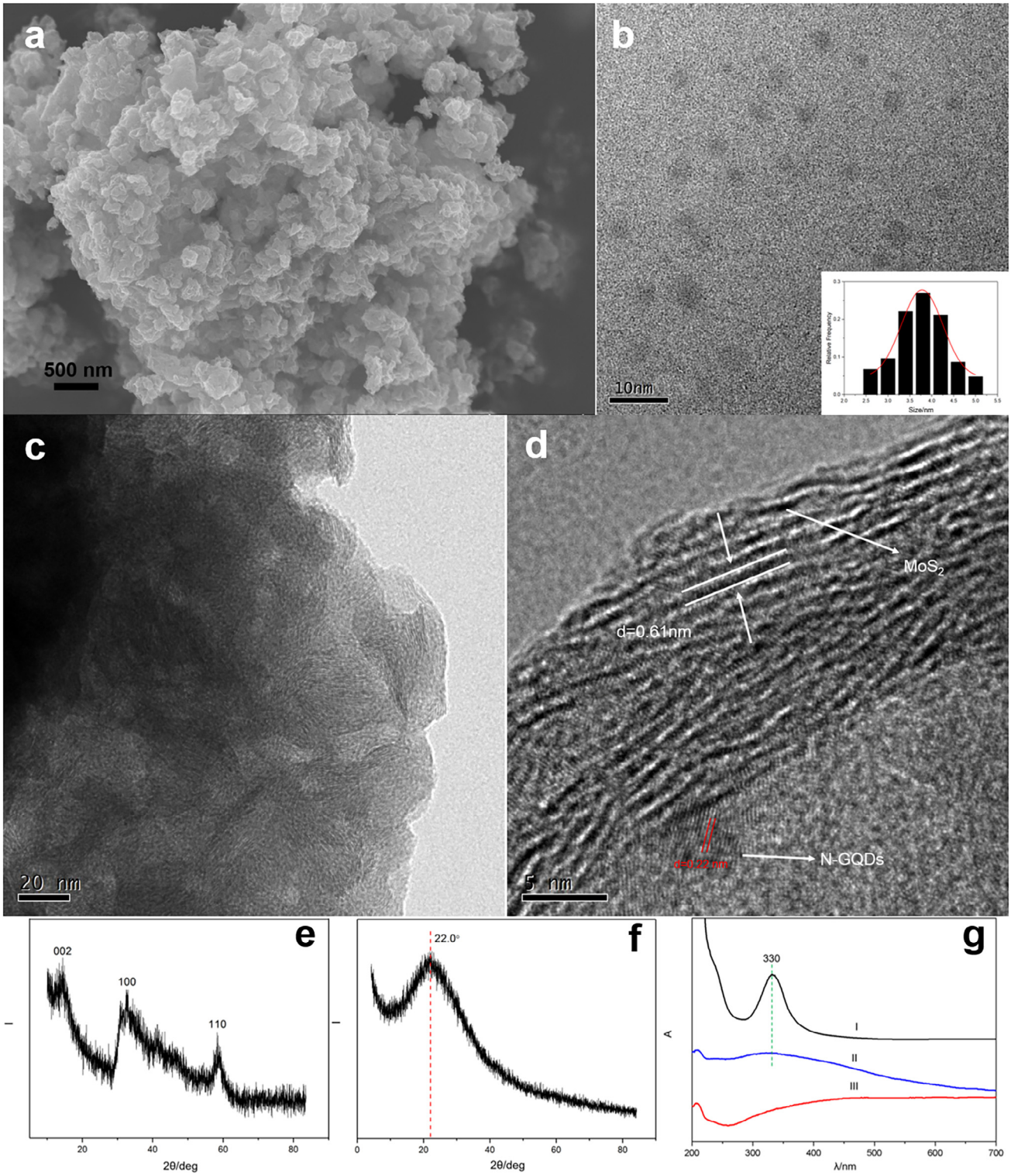

Fig. 1. (a) SEM images of MoS_2@N-GQDs-IL. (b) TEM image for those N-GQDs. (c) TEM image of MoS_2-IL. (d) HRTEM of MoS_2@N-GQDs-IL. (e) XRD patterns of MoS_2@N-GQDs-IL. (f) XRD patterns of N-GQDs. (g) UV–vis spectra for N-GQDs (I), MoS_2@N-GQDs-IL (II), and MoS_2-IL (III).

TEM image is shown in Fig. 1c. As observed, the IL covalent functionalization offered a molecule layer onto those composites. Fig. 1d shows the high-resolution TEM (HRTEM) image for MoS_2@N-GQDs-IL. Clearly, there were a few layers in MoS_2 with layered structure, and the distance between two layers was 0.62 nm. Obviously, those quantum dots synthesized according to our approach displayed great crystallinity, with a 0.22 nm lattice spacing, which was indexed to the (1 1 2 0) graphene lattice fringes [64]. Fig. 1e suggested that, there were only 3 weak diffraction peaks of MoS_2@N-GQDs-IL composites, which were corresponding to (1 1 0), (1 0 0), and (0 0 2) MoS_2 planes, and such results indicated poor MoS_2 crystallinity. This phenomenon was ascribed to the fact that, incorporating N-GQDs inhibited the growth of layered MoS_2 crystal in the hydrothermal process. Fig. 1f shows the XRD pattern

of N-GQDs, the 2 theta angles ranged from 5° to 85°, with a characteristic peak of 22.0°, which was consistent with the graphite structure of N-GQDs reported in the literature [65], indicating that N-GQDs were prepared successfully.

UV–vis spectroscopy was carried out to characterize the products. Fig. 1g revealed that, the characteristic peaks for MoS_2@N-GQDs-IL composite and N-GQDs were observed at 330 nm, respectively. In addition, MoS_2-IL had no characteristic peak at 330 nm, indicating that N-GQDs were attached to the MoS_2-IL.

3.2. Electrochemical performances of the MoS_2@N-GQDs-IL composites

EIS is developed as a highly efficient approach to probe into those surface-modified electrode features [66–69]. Specifically, those impedance spectra are comprised of the linear portion and the semicircle portion. Besides, the high-frequency semicircle diameter is corresponding to the resistance of electron transfer (R_{et}), whereas the low frequency linear part is associated with a diffusion event [70,71]. Fig. 2 shows various electrode electron transfer capacities and relevant results. Clearly, bare GCE had a low semicircle EIS at a high frequency; in addition, the linear portion was observed at a lower frequency (curve a), which suggested a quite low R_{et} to the $[Fe(CN)_6]^{3-/4-}$ redox probe. Nonetheless, as observed from the EIS analysis for MoS_2@N-GQDs-IL/GCE (curve d), MoS_2@N-GQDs/GCE (curve c), and MoS_2/GCE (curve b), nearly straight lines were seen within the Nyquist plot, indicating the little charge transfer impedance of these sensors. Further, the electrode process was mainly controlled by the diffusion process, rather than the charge transfer. In addition, the AC impedance spectrum indicated that the bare electrode (curve a) had a high charge transfer impedance, which was remarkably low in the modified sensor, demonstrating that both of them had superb electron conductivity. On the other hand, the above AC impedance spectrum strongly proved the successful modification of MoS_2, MoS_2@-N-GQDs together with MoS_2@N-GQDs-IL onto the electrode surface.

Fig. 3 illustrates the $[Fe(CN)_6]^{3-/4-}$ behaviors on the surface of various modified electrodes and GCE. The bare GCE displayed a good reversible redox reaction (curve a). Compared with bare GCE, MoS_2/GCE (curve b) showed an increased peak current due to the conductivity of MoS_2. MoS_2@N-GQDs/GCE (curve c) presented the higher peak current than that of MoS_2/GCE (curve b), which was mainly on account of N-GQDs as a good conductivity agent to enhance the electron transfer. In comparison with MoS_2@N-GQDs/GCE (curve c), MoS_2/GCE (curve b), and GCE (curve a), MoS_2@N-GQDs-IL/GCE (curve d) had the greatest peak current, suggesting that the ability of MoS_2@N-GQDs-IL to be a sensitive element in electrochemical sensor fabrication. MoS_2@N-GQDs-IL membrane had electronic performances and required surface for supporting the quick electron transfer of the redox system, which was complicated mechanistically.

3.3. MIPs NPs characterizations

3.3.1. High resolution transmission microscopy

MIPs NPs, together with the $CuFe_2O_4$ NPs, were investigated using HRTEM, so as to verify the distribution of polymer coating, surface and structure. For $CuFe_2O_4$ NPs (Fig. 4a), the spherical shape was observable, and the mean size was 160 nm. In the case of MIPs NPs, (Fig. 4b) the $CuFe_2O_4$ NPs were surrounded by an imprinted layer. The imprinted layer had a thin edge of 15 nm, which was conductive to the elution and absorption of the template protein.

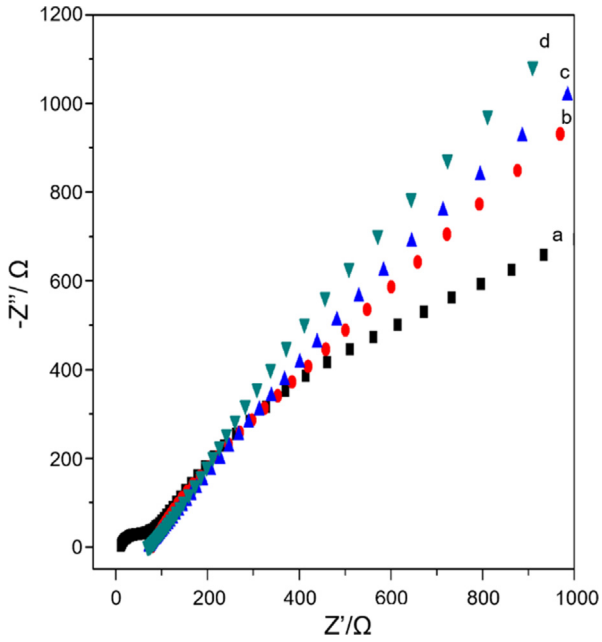

Fig. 2. Nyquist plots at GCE (a), MoS_2/GCE (b), MoS_2@N-GQDs/GCE (c), and MoS_2@-N-GQDs-IL/GCE (d) in PBS (pH = 7.4) containing 5 mmol·L^{-1} $K_3Fe(CN)_6$ and 0.1 mol·L^{-1} KCl.

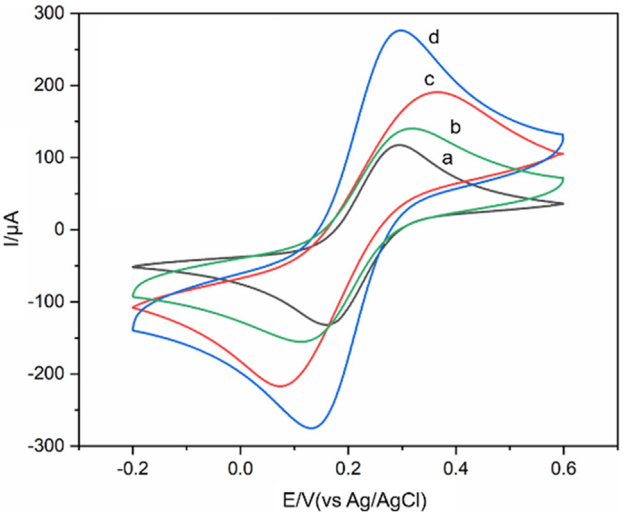

Fig. 3. Cyclic voltammograms for GCE (a), MoS_2/GCE (b), MoS_2@N-GQDs/GCE (c) and MoS_2@N-GQDs-IL/GCE (d) in PBS (pH = 7.4) containing 5 mmol·L^{-1} $K_3Fe(CN)_6$ and 0.1 mol·L^{-1} KCl (scan rate: 100 mV/s).

3.3.2. Fourier transform infrared spectroscopy

FT-IR spectra of MIPs NPs before template extraction, MIPs NPs after template extraction and NIPs NPs are presented in Fig. 5. Based on those spectra for MIPs NPs as well as NIPs NPs, the Fe—O peak was at 581 cm^{-1} and the broadband was centered at 3392 cm^{-1} due to O—H stretching overlap. With regard to the FT-IR spectra for MIPs NPs (curve a, b), the peak at 1405 cm^{-1} was carboxyl, which was used to synthesize $CuFe_2O_4$ magnetic nanoparticles. Comparing the FT-IR spectra for NIPs NPs (curve c), it was discovered the characteristic absorption peak of IgG (Fig. 5) at 1590 cm^{-1} amide bond also appeared on the infrared spectra of MIPs NPs before template extraction (curve a). This phenomenon represented that IgG was successfully encapsulated, which suggested the successful preparation of imprinted complex. Compared the FT-IR spectra for MIPs NPs before template extrac-

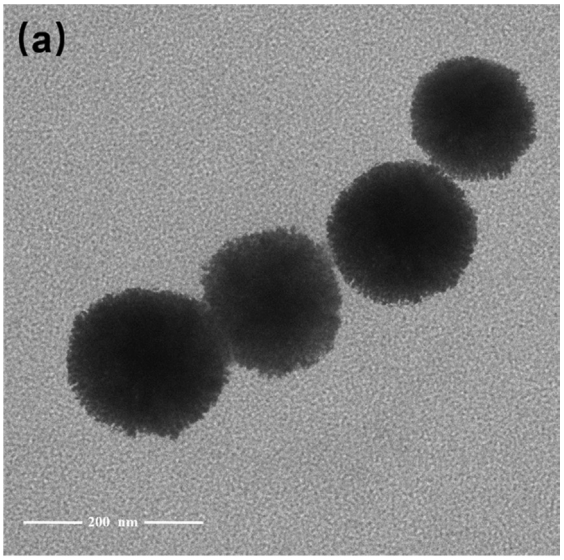

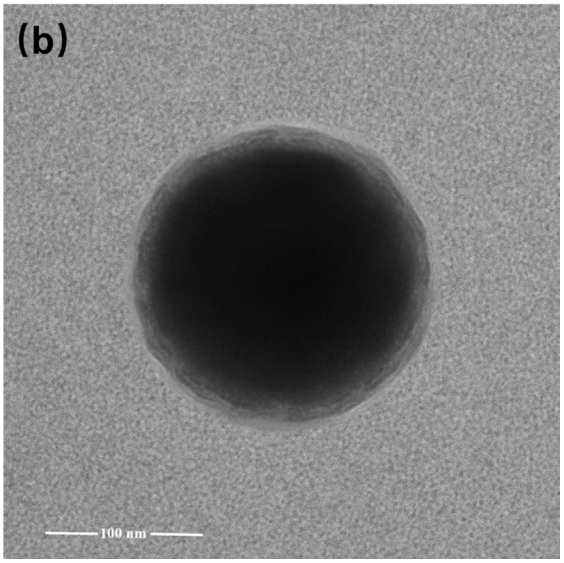

Fig. 4. HRTEM photographs of $CuFe_2O_4$ NPs (a) and MIPs NPs (b).

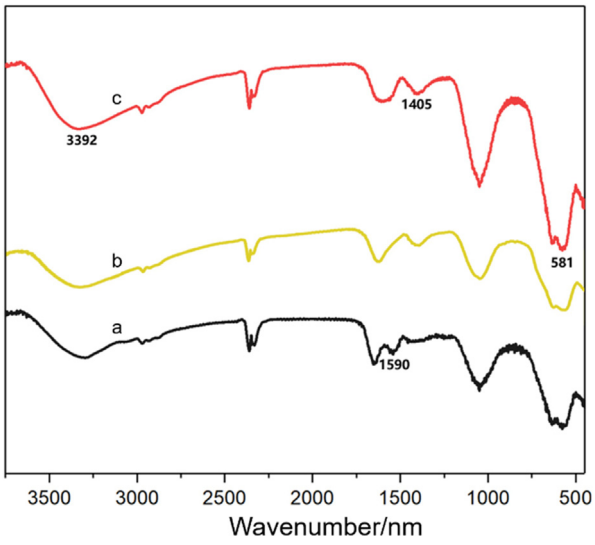

Fig. 5. FT-IR spectra of MIPs NPs before template extraction (a), MIPs NPs after template extraction (b) and NIPs NPs (c).

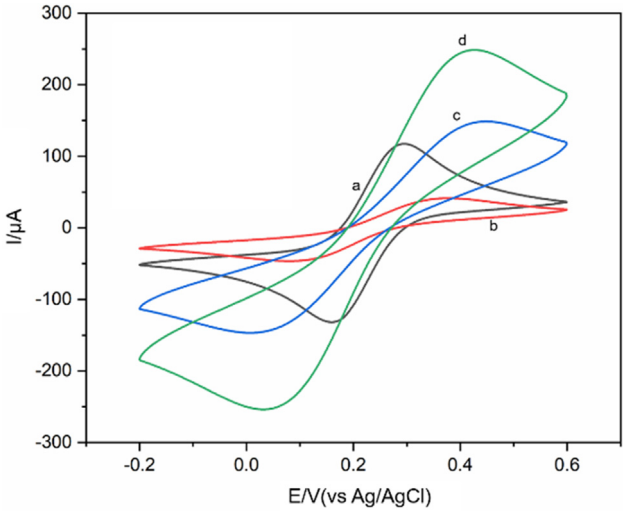

Fig. 6. CV curves for different electrodes in PBS (pH = 7.4) containing 5 mmol·L^{-1} $K_3Fe(CN)_6$ and 0.1 mol·L^{-1} KCl, GCE (a), MIPs NPs/MoS_2@N-GQDs-IL/GCE before removing IgG (b), MIPs NPs/MoS_2@N-GQDs-IL/GCE after binding IgG (c), and MIPs NPs/MoS_2@N-GQDs-IL/GCE after removing IgG(d) (scan rate: 100 mV/s).

tion (curve a), there was no 1590 cm^{-1} band on the infrared spectra of MIPs NPs after template extraction (curve b), indicating the completeness of this extraction.

3.3.3. Electrochemical characterization

The diverse electrodes were electrochemically characterized by cyclic voltammetric measurements within the PBS containing 5 mmol·L^{-1} [$K_3Fe(CN)_6$] and 0.1 mol·L^{-1} KCl. Fig. 6 presents the CV distribution of bare GCE and different modified electrodes. As shown, bare GCE had one pair of reversible redox peaks (curve a). For the electrode modified with MIPs NPs materials before removing the template, it was difficult for the ferrocyanide anions to enter the electrode surface, due to the poor electron transport of the dense membrane. As a result, the intensity of the electrochemical signals was significantly shortened (curve b). After removing the template from the MIPs NPs matrix, the current response sharply increased, indicating that probe molecules diffused to the electrode surface through cavity regeneration (curve d), which invoked the so-called 'gate effect' [72]. At last, the MIPs NPs/MoS_2@N-GQDs-IL/GCE after binding IgG (curve c) showed that the peak current decreased relative to curve d. This was called cavity occupation (sites of recognition) by IgG.

3.4. Experimental condition optimization

3.4.1. Effects of the concentration and volume

This study investigated influences of experimental variables on oxidation peak current (I_p) for the 1 ng·mL^{-1} IgG on the imprinted GCE using the DPV mode, due to its great resolution and sensitivity.

The volume and content of the as-prepared MIPs NPs dispersion that was dripped onto GCE surface greatly affected the sensor selectivity and sensitivity, as presented in Fig. 7a and b. Clearly, I_p remarkably changed as the volume or content of the as-prepared MIPs NPs dispersion altered. Typically, I_p peaked in the 10 μL MIPs NPs dispersion (3 mg/mL). As the dispersion volume and content increased, the number of IgG binding sites elevated.

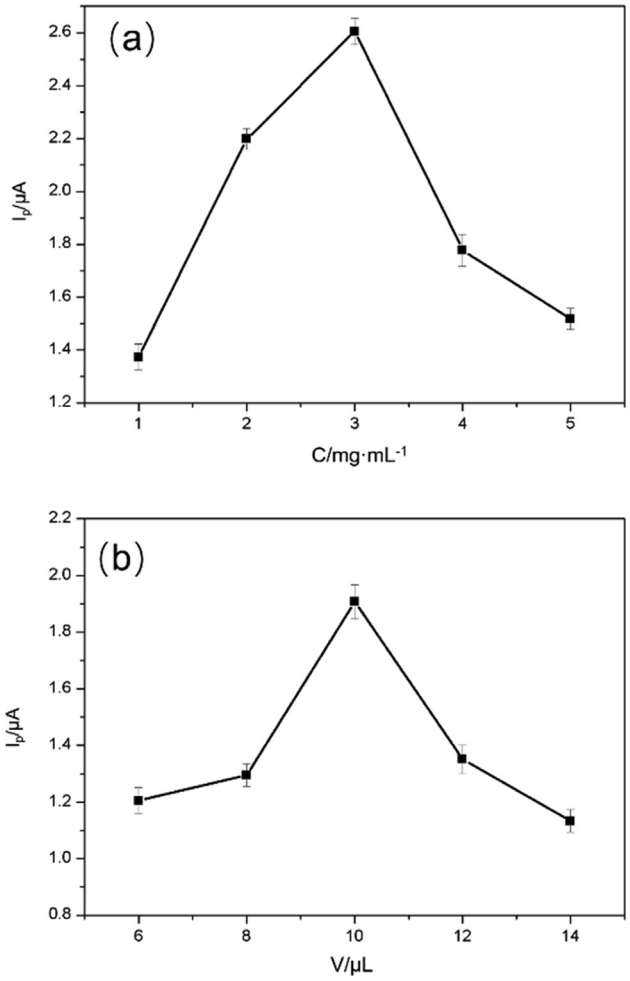

Fig. 7. Impacts of the MIPs NPs dispersion content (a) and volume (b). The differential pulse voltammetry (DPV) conditions: pulse width was 0.05 s, pulse amplitude was 50 mV, and scan rate was 100 mV/s, electrolyte solution was PBS (pH = 7.4) with 1 ng·mL^{-1} IgG. Error bar = RSD (n = 3).

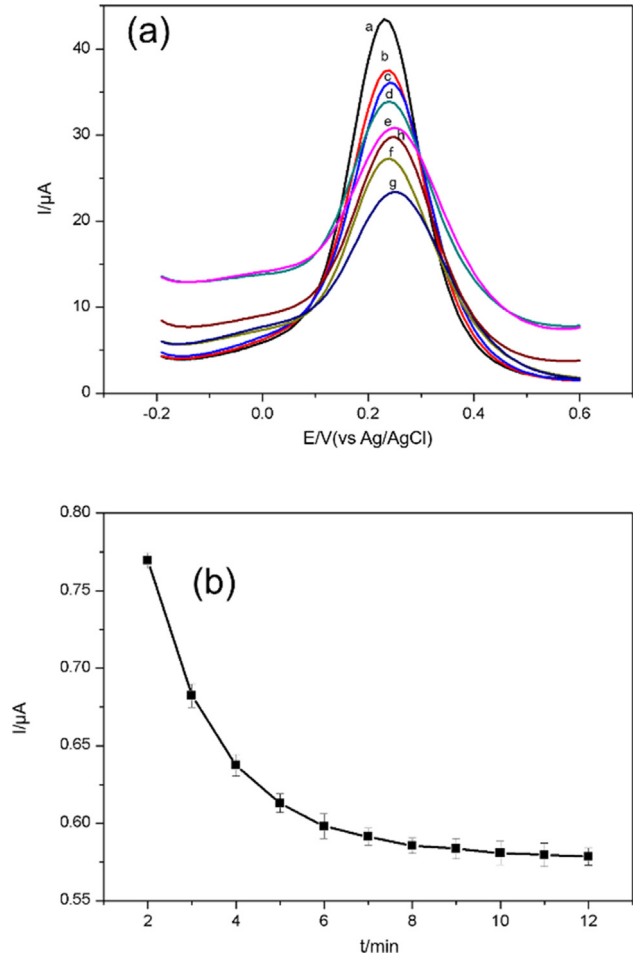

Fig. 8. (a) Differential pulse voltammetry in PBS (pH = 7.4) containing 5 mmol·L^{-1} $K_3[Fe(CN)_6]$ at MIPs NPs/MoS_2@N-GQDs-IL/GCE for varied incubation times. The differential pulse voltammetry (DPV) conditions: pulse width was 0.05 s, pulse amplitude was 50 mV, and scan rate was 100 mV/s. (a → h: 2 → 9 min) (b) Effects of incubation time on the oxidation response to IgG for MIPs NPs/MoS_2@N-GQDs-IL/GCE. Error bar = RSD (n = 3).

As a result, the presence of a large or low amount of modified MIPs NPs on the sensor surface reduced the IgG response.

3.4.2. Incubation time

Incubation time serves as the vital index to evaluate the sensitivity for the MIP sensor. As a result, this study investigated how incubation time affected the MIPs NPs responses by DPV within the PBS (pH = 7.4) containing 5 mmol·L^{-1} $K_3[Fe(CN)_6]$. Thereafter, the molecularly imprinted electrochemical sensor was used to remove those template molecules, followed by immersion with PBS buffer supplemented with 1 ng·mL^{-1} IgG standard solution for various time periods. According to Fig. 8, the peak current quickly shortened within the first 8 min, which indicated that those binding sites of the sensor were able to quickly and effectively adsorb IgG molecules. After 8 min, the peak current decreased slowly and remained almost unchanged, which suggested the state of adsorption equilibrium reached by the imprinted sensor. In this study, the adsorption equilibrium peaked in 8 min, and such quick response was ascribed to the surface imprinting.

3.5. MIPs NPs detectability in detecting IgG

Under the optimum condition, the sensor was employed to detect IgG in PBS (pH = 7.4) after incubating it for 8 min (Fig. 9a). Fig. 9b presents a linear calibration curve for IgG oxidation within the specific content range (0.1–50 ng·mL^{-1}). Typically, the MIPs NPs detectability was detected within 0.1–50 ng·mL^{-1} IgG, and the determined LOD (S/N = 3) was 0.02 ng·mL^{-1}. Further, that regression equation obtained was I(μA) = 1.6211 lgC (ng·mL^{-1}) + 9.1457, (R^2 = 0.998). In addition, the comparisons of several reported analytical techniques for detecting human IgG are listed in Table 1. As seen, the proposed method has comparable or even better limit of detection and linear concentration range. The research results suggested that this advanced molecularly imprinted electrochemical sensor can be used as an immunosensor for the determination of human IgG in serum samples.

3.6. Measurement reproducibility

To verify the reproducibility of our adopted approach, the calibration curves were repeated for three times by measuring the DPV response of a 1 ng·mL^{-1} IgG solution using five independently electrodes under the same conditions. In addition, the values of relative standard deviation (RSD%) were compared between 2% and 5%, and the results suggested acceptable reproducibility of those electrodes.

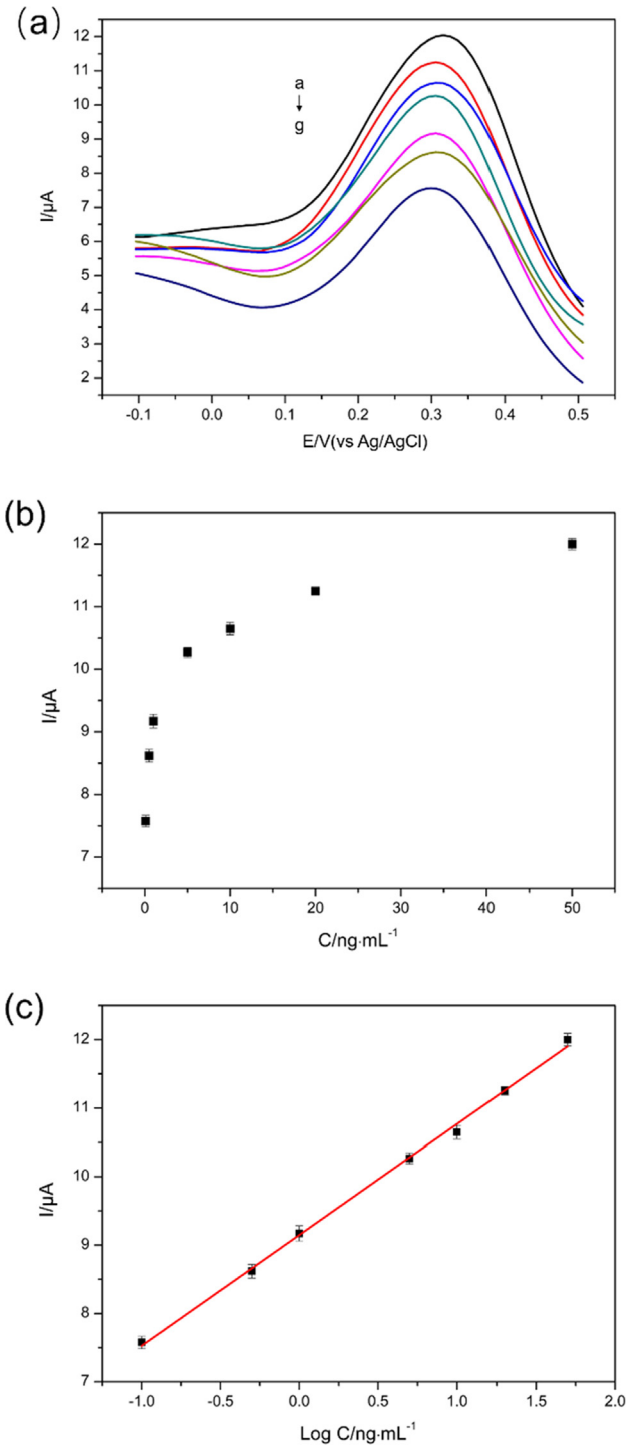

Fig. 9. (a) Differential pulse voltammograms of MIPs NPs/MoS_2@N-GQDs-IL/GCE electrode in PBS (pH = 7.4) with different concentrations (a → g: 0.1, 0.5, 1, 5, 10, 20 and 50 ng·mL^{-1}). Scan rate: 100 mV/s. (b and c) Calibration curves for human IgG at MIPs NPs/MoS_2@N-GQDs-IL/GCE. Error bar = RSD (n = 3).

3.7. Measurement stability

Adsorption values for the modified imprinted electrodes on 1 ng·mL^{-1} IgG exhibited no substantial change among various time periods, which verified the method stability. Those modified imprinted electrodes were put into the ultra-pure water for 2 weeks under ambient temperature. Then, the DPV response was measured every three days. The IgG peak current response for the imprinted electrodes was shortened to 93.4%, which indicated the favorable long-term stability and reusability of the electrode.

3.8. Selectivity analysis

To evaluate the selectivity of the sensor in target identification, several representative interferers that were commonly used in the actual sample detection process were selected in the experiment, so as to detect the sensor selectivity. To be specific, HSA, BSA and Lyz were selected as the interferers in the experiment. Under the optimal conditions, DPV responses of the proposed MIP or NIP in different concentrations (0.5, 1, 5, 20 and 50 ng·mL^{-1}) IgG solutions with or without interferences were assayed.

We have obtained the calculation method of imprinting factor and selectivity coefficient through Refs. [77,78]. The imprinting factor should be determined from the ratio of slopes of calibration plots for MIP sensor (0.354 μA/ ng·mL^{-1}) (Table 2) and NIP sensor (0.021 μA/ ng·mL^{-1}) (Table 2). The imprinting factor was 16.9. Moreover, the selectivity coefficient to each interfering compound could be determined as the ratio of the slope of the calibration plot for IgG and a given compound including HSA, BSA and Lyz (Fig. 10, Table 2). And the calculated selectivity coefficient of HSA, BSA and Lyz were 7.4, 8.4 and 9.3 respectively. Advantageously, the sensor did not respond to HSA, BSA and Lyz. Consequently, the as-prepared IgG biosensor in this study exhibited favorable selectivity for the target IgG. Such an experimental result showed that the biosensor might be used in accurately measuring IgG concentration within practical specimens.

3.9. IgG content measurements within the clinic blood samples

For healthy people, the IgG content within the serum is 8.0–16.0 mg·mL^{-1}.

In this study, 3 whole blood specimens were obtained from the hospital physic examination center. After complete coagulation, the blood was centrifuged at 3500 r/min for 10 min to collect the upper serum. The blood serum specimens were diluted with PBS at the ratio of 1:200000 prior to analysis. The German SIEMENS BN II automatic protein analyzer (immune nephelometry) was used to detect serum IgG, whereas the values were 25.5, 27.0, and 37.5 ng·mL^{-1}, separately. The above three specimens were measured with this sensor, and the IgG contents were 27.1, 28.3, and 36.7 ng·mL^{-1}, respectively. The results were compared with the reference values obtained by immune nephelometry method as shown in Table 3. The relative deviation (%) between the electrochemical immunosensors and immune nephelometry method ranged from −6.3% to 2.1%. Typically, the IgG contents measured using

Table 1
Comparison of the proposed method with previously reported analytical techniques.

Immunosensor	Linearity (ng·mL^{-1})	Detection limit (ng·mL^{-1})	Ref.
ZnO/chitosan composite	2.5–500	1.2	[73]
Ab/DAC/GCE	0.5–45	0.3	[74]
ZnO@ZIF-8/IL	0.1–10, 10–400	0.03	[21]
Protein A modified gold electrode	10–1000	5	[75]
GR-GR-MWCT	1–500	0.2	[76]
MoS_2@N-GQDs-IL MIP Sensors	0.1–50	0.02	This work

Table 2
Analytical parameters of the MIP sensor for IgG.

Name	MIP-IgG	NIP-IgG	MIP-HSA	MIP-BSA	MIP-Lyz
Slope	0.354 ± 0.024	0.021 ± 0.004	0.048 ± 0.014	0.042 ± 0.006	0.038 ± 0.008
Intercede	33.428 ± 0.615	1.978 ± 0.052	1.592 ± 0.402	1.049 ± 0.068	2.013 ± 0.169

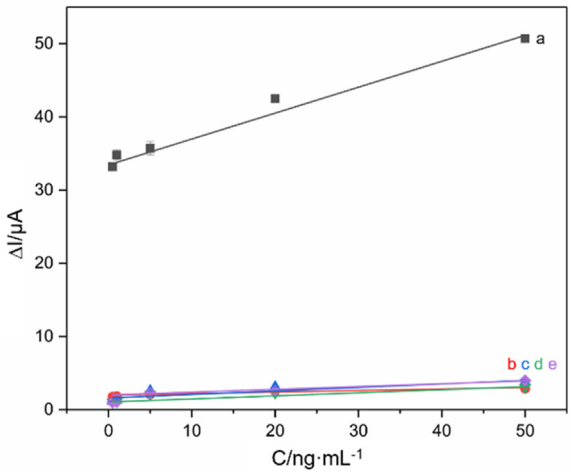

Fig. 10. Calibration plots for the MIP (a), NIP (b), and the interferences (c – HSA, d – BSA, and e - Lyz) with MIP in PBS (pH = 7.4) containing 5 mmol·L^{-1} [$K_3Fe(CN)_6$].

Table 3
Results of determination of IgG in real serum samples.

Serum Sample	Immunosenor (ng·mL^{-1})	RSD (n = 3) %	Immune nephelometry (ng·mL^{-1})	Relative deviation (%)
1	27.1	2.9	25.5	−6.3
2	28.3	3.3	27.0	−4.8
3	36.7	5.3	37.5	2.1

Table 4
Analytical results of IgG in real serum samples after dilution.

Sample	Orignal (ng·mL^{-1})	Added (ng·mL^{-1})	Found (ng·mL^{-1})	Recovery %	RSD (n = 3) %
1	27.1	10	35.1	94.6	5.1
2	28.3	10	39.0	101.8	3.7
3	36.7	10	46.0	98.5	4.2

the as-proposed IgG sensor were in line with those protein analyzer values. Besides, human serum specimens with spiked IgG contents were adopted for validating our method. The recovery rates ranged from 94.6% to 101.8%. Table 4 present the determined results for 3 distinct specimens and the recovery rates.

4. Conclusions

This study successfully prepares the layered MoS_2@N-GQDs-IL nanocomposite membrane, and first adopts it as the support matrix to construct the electrochemical sensor for IgG. As observed, the MoS_2@N-GQDs-IL/GCE system has markedly increased peak current, demonstrating that the MoS_2@N-GQDs-IL composite membrane plays a role as a highly effective promoter in enhancing the IgG electrochemical performance. In addition, MIPs NPs are then modified onto GCE surface to develop the new electrochemical sensor, so as directly determine the IgG level. Notably, the developed electrochemical sensor can selectively recognize IgG, meanwhile, it shows great reliability and accuracy, quick response time, and favorable reproducibility. Our research results reveal that the developed IgG sensor is successfully used for analyzing IgG content in the human serum specimens, which may show promising clinical applications to detect the IgG content.

Declaration of Competing Interest

The authors declare that they have no known competing financial interests or personal relationships that could have appeared to influence the work reported in this paper.

Acknowledgement

The primary funders and grant IDs is the National Key R&D Program of China (Grant No. 2019YFA0904104).

References

[1] M. Sanda, R. Goldman, Data Independent analysis of IgG glycoforms in samples of unfractionated human plasma, Anal. Chem. 88 (2016) 10118–10125.
[2] E.U. Patel, S. Gianella, K. Newell, A.A.R. Tobian, A.R. Kirkpatrick, F. Nalugoda, M. K. Grabowski, R.H. Gray, D. Serwadda, T.C. Quinn, A.D. Redd, S.J. Reynolds, Elevated cytomegalovirus IgG antibody levels are associated with HIV-1 disease progression and immune activation, AIDS 31 (2017) 807–813.
[3] B.M. Chen, Y.C. Su, C.J. Chang, P.A. Burnouf, K.H. Chuang, C.H. Chen, T.L. Cheng, Y.T. Chen, J.Y. Wu, S.R. Roffler, Measurement of pre-existing IgG and IgM antibodies against polyethylene glycol in healthy individuals, Anal. Chem. 88 (2016) 10661–10666.
[4] F. Finger-Jardim, E.C. Avila, V.P. da Hora, P.C.D. Santos, C.V. Gonçalves, G. Mor, A.M.B. de Martinez, M.A. Soares, Herpes simplex virus type 2 IgG antibodies in sera of umbilical cord as a proxy for placental infection in asymptomatic pregnant women, Am. J. Reprod. Immunol. 79 (2018) e12824.
[5] E.P. Mcguire, Y. Fong, C. Toote, C.K. Cunningham, G.G. Fouda, HIV exposed infants vaccinated with a MF59/rgp120 vaccine have higher magnitude anti-V1V2 IgG responses than adults immunized with the same vaccine, J. Virol. 92 (2017), e01070-17.
[6] M.G. Derebe, R.K. Nanjunda, G.L. Gilliland, E.R. Lacy, M.L. Chiu, Human IgG subtype cross-species reactivity to mouse and cynomolgus monkey Fcγ receptors, Immunol. Lett. 197 (2018) 1–8.
[7] J. Sabín, G. Prieto, J.M. Ruso, P.V. Messina, F.J. Salgado, M. Nogueira, M. Costas, Félix Sarmiento, Interactions between DMPC Liposomes and the Serum Blood Proteins HSA and IgG, J. Phys. Chem. B 113 (2009) 1655–1661.
[8] G. VogelMar, New blood tests for antibodies could show true scale of coronavirus pandemic.Science|AAAS, 2020. https://www.sciencemag.org/news/2020/03/new-blood-tests-antibodies-could-show-true-scale-coronavirus-pandemic.
[9] M. Guy, H.B.C. Bremer, B. Tapan, M. Tegwen, S.O. Prakash, M. Pascal, K.F. Andrew, El-Safi Sayda, Detection of immunoglobulin g1 against rk39 improves monitoring of treatment outcomes in visceral leishmaniasis, Clin. Infect. Dis. 7 (2018) 1130–1135.
[10] S.E.D. Jong, M.H.J. Selman, A.A. Adegnika, A.S. Amoah, M. Yazdanbakhsh, IgG1 Fc N-glycan galactosylation as a biomarker for immune activation, Sci. Rep. 6 (2016) 28207.
[11] J. Bodle, E.E. Verity, C. Ong, K. Vandenberg, R. Shaw, I.G. Barr, S. Rockman, Development of an enzyme-linked immunoassay for the quantitation of influenza haemagglutinin: an alternative method to single radial immunodiffusion, Influenza Other Resp. 7 (2013) 191–200.
[12] Y. Iizumi, T. Okazaki, Y. Ikehara, M. Ogura, S. Fukata, M. Yudasaka, Immunoassay with single-walled carbon nanotubes as near-infrared fluorescent labels, ACS Appl. Mater. Interfaces 5 (2013) 7665–7670.
[13] F. Peng, X.P. Xu, L. Wang, C.M. Ying, Comparison on the anti-interference abilities of immune turbidimetry and immune nephelometry for detecting specific proteins, Lab. Med. 28 (2013) 142–145.
[14] N.V. Beloglazova, P.S. Shmelin, E.S. Speranskaya, B. Lucas, C. Helmbrecht, D. Knopp, R. Niessner, S. De Saeger, I.Y. Goryacheva, Quantum dot loaded liposomes as fluorescent labels for immunoassay, Anal. Chem. 85 (2013) 7197–7204.

[15] S.D. Gan, K.R. Patel, Enzyme immunoassay and enzyme-linked immunosorbent assay, J. Invest. Dermatol. 133 (2013) e12.
[16] N.E. Pollok, C. Rabin, L. Smith, R.M. Crooks, Orientation-controlled bioconjugation of antibodies to silver nanoparticles, Bioconjug. Chem. 30 (2019) 3078–3086.
[17] A. Teimouri, M.H. Modarressi, S. Shojaee, M. Mohebali, H. Keshavarz, Detection of toxoplasma-specific immunoglobulin g in human sera: performance comparison of in house dot-elisa with eclia and elisa, Eur. J. Clin. Microbiol. 37 (2018) 1–9.
[18] R. Elshafey, A.C. Tavares, M. Siaj, M. Zourob, Electrochemical impedance immunosensor based on gold nanoparticles–protein G for the detection of cancer marker epidermal growth factor receptor in human plasma and brain tissue, Biosens. Bioelectron. 50 (2013) 143–149.
[19] W. Liang, W. Yi, S. Li, R. Yuan, A.n. Chen, S. Chen, G. Xiang, C. Hu, A novel, label-free immunosensor for the detection of α-fetoprotein using functionalised gold nanoparticles, Clin. Biochem. 42 (2009) 1524–1530.
[20] P. Mashazi, P. Tetyana, S. Vilakazi, T. Nyokong, Electrochemical impedimetric immunosensor for the detection of measles-specific IgG antibodies after measles infections, Biosens. Bioelectron. 49 (2013) 32–38.
[21] S. Dong, M. Tong, D. Zhang, T. Huang, The strategy of nitrite and immunoassay human IgG biosensors based on ZnO@ZIF-8 and ionic liquid composite film, Sensor. Actuat. B-Chem. 251 (2017) 650–657.
[22] R. Li, K. Wu, C. Liu, Y. Huang, Y. Wang, H. Fang, H. Zhang, C. Li, 4-Amino-1-(3-mercapto-propyl)-pyridine hexafluorophosphate ionic liquid functionalized gold nanoparticles for IgG immunosensing enhancement, Anal. Chem. 86 (2014) 5300–5307.
[23] H.C.W. Hays, P.A. Millner, M.I. Prodromidis, Development of capacitance based immunosensors on mixed self-assembled monolayers, Sensor. Actuat. B-Chem. 114 (2016) 1064–1070.
[24] Q.G. He, J. Liu, X.P. Liu, G.L. Li, P.H. Deng, J. Liang, Preparation of Cu_2O-reduced graphene nanocomposite modified electrodes towards ultrasensitive dopamine detection, Sensors 18 (2018) 199.
[25] Q.G. He, J. Liu, X.P. Liu, G.L. Li, D.C. Chen, P.H. Deng, J. Liang, Fabrication of amine-modified magnetite-electrochemically reduced graphene oxide nanocomposite modified glassy carbon electrode for sensitive dopamine determination, Nanomaterials 8 (2018) 194.
[26] Q.G. He, Y.Y. Wu, Y.L. Tian, G.L. Li, L. Jun, P.H. Deng, D.C. Chen, Facile electrochemical sensor for nanomolar rutin detection based on magnetite nanoparticles and reduced graphene oxide decorated electrode, Nanomaterials 9 (2019) 115.
[27] Y.L. Tian, P.H. Deng, Y.Y. Wu, J.H. Li, J. Liu, G.L. Li, Q.G. He, MnO_2 nanowires-decorated reduced graphene oxide modified glassy carbon electrode for sensitive determination of bisphenol a, J. Electrochem. Soc. 167 (2020) 046514.
[28] Y.L. Tian, P.H. Deng, Y.Y. Wu, J. Liu, J.H. Li, G.L. Li, Q.G. He, High sensitive voltammetric sensor for nanomolarity vanillin detection in food samples via manganese dioxide nanowires hybridized electrode, Microchem. J. 157 (2020) 104885.
[29] K. Chang, W. Chen, In situ synthesis of MoS_2/graphene nanosheet composites with extraordinarily high electrochemical performance for lithium ion batteries, Chem. Commun. 47 (14) (2011) 4252–4254.
[30] M.T. Manzoor, V.H. Nguyen, S. Umrao, Mutually exclusive pmilype and nmilype hybrid electrode of MoS2 and graphene for artificial soft touch fingers, Adv. Funct. Mater. 29 (2019) 2905454.
[31] Y.F. Sun, J.B. He, G.I.N. Waterhouse, L.H. Xu, H.Y. Zhang, X.G. Qiao, Z.X. Xu, A selective molecularly imprinted electrochemical sensor with GO@COF signal amplification for the simultaneous determination of sulfadiazine and acetaminophen, Sensor. Actuat. B-Chem. 300 (2019) 126993.
[32] B. Hatamluyi, A. Hashemzadeh, M. Darroudi, A novel molecularly imprinted polymer decorated by CQDs@HBNNS nanocomposite and UiO-66-NH2 for ultra-selective electrochemical sensing of Oxaliplatin in biological samples, Sensor. Actuat. B-Chem. (2020), https://doi.org/10.1016/j.snb.2019.127614.
[33] S. Zhu, J. Zhang, C. Qiao, S. Tang, Y. Li, W. Yuan, B. Li, L. Tian, F. Liu, R. Hu, H. Gao, H. Wei, H. Zhang, H. Sun, B. Yang, Chem. Commun. 47 (2011) 6859–6860.
[34] A.P.P. Eisele, C.F. Valezi, T. Mazziero, R.F.H. Dekker, A.M. Barbosa-Dekker, E.R. Sartori, Layering of a film of carboxymethyl-botryosphaeran onto carbon black as a novel sensitive electrochemical platform on glassy carbon electrodes for the improvement in the simultaneous determination of phenolic compounds, Sensor. Actuat. B-Chem. 287 (2019) 18–26.
[35] A. Wong, A.M. Santos, O. Fatibello-Filho, Simultaneous determination of paracetamol and levofloxacin using a glassy carbon electrode modified with carbon black, silver nanoparticles and PEDOT:PSS film, Sensor. Actuat. B-Chem. 255 (2018) 2264–2273.
[36] X. Qiao, K. Li, J. Xu, N.i. Cheng, Q. Sheng, W. Cao, T. Yue, J. Zheng, Novel electrochemical sensing platform for ultrasensitive detection of cardiac troponin I based on aptamer-MoS_2 nanoconjugates, Biosens. Bioelectron. 113 (2018) 142–147.
[37] H. Huang, M. Wang, Y. Wang, X. Li, Z. Niu, X. Wang, J. Song, Electrochemical determination of 2,4-dichlorophenol by using a glassy carbon electrode modified with molybdenum disulfide, ionic liquid and gold/silver nanorods, Microchim. Acta 185 (2018) 292.
[38] K.-J. Huang, L. Wang, J. Li, Y.-M. Liu, Electrochemical sensing based on layered MoS_2–graphene composites, Sensor. Actuat. B-Chem. 178 (2013) 671–677.
[39] Y.-I. Yao, Y.a. Ding, L.-S. Ye, X.-H. Xia, Two-step pyrolysis process to synthesize highly dispersed Pt–Ru/carbon nanotube catalysts for methanol electrooxidation, Carbon 44 (2006) 61–66.
[40] G.C. Huang, T. Chen, W.X. Chen, Z. Wang, K. Chang, L. Ma, F.H. Huang, D.Y. Chen, J.Y. Lee, Graphene-like MoS_2/graphene composites: cationic surfactant-assisted hydrothermal synthesis and electrochemical reversible storage of lithium, Small 9 (21) (2013) 3693–3703.
[41] T. Guo, L. Wang, S. Sun, Y. Wang, X. Chen, K. Zhang, D. Zhang, Z. Xue, X. Zhou, Layered MoS_2@graphene functionalized with nitrogen-doped graphene quantum dots as an enhanced electrochemical hydrogen evolution catalyst, Chinese Chem. Lett. 30 (2019) 1253–1260.
[42] J.M. Gomes, S.S. Silva, R.L. Reis, Biocompatible ionic liquids: fundamental behaviours and applications, Chem. Soc. Rev. 48 (2019) 4317–4335.
[43] J. Tang, H. Song, X. Feng, A. Yohannes, S. Yao, Ionic liquid-like pharmaceutical ingredients and applications of ionic liquids in medicinal chemistry: development, status and prospects, CMC 26 (32) (2019) 5947–5967.
[44] R.T. Kachoosangi, M.M. Musameh, I. Abu-Yousef, J.M. Yousef, S.M. Kanan, L. Xiao, S.G. Davies, A. Russell, R.G. Compton, Carbon nanotube−ionic liquid composite sensors and biosensors, Anal. Chem. 81 (2009) 435–442.
[45] C.I.L. Justino, A.C. Freitas, R. Pereira, A.C. Duarte, T.A.P.R. Santos, Trac-Trend. Anal. Chem. 68 (2015) 2–17.
[46] Q. He, J. Liu, X. Liu, G. Li, D. Chen, P. Deng, J. Liang, A promising sensing platform toward dopamine using MnO2 nanowires/electro-reduced graphene oxide composites, Electrochim. Acta 296 (2019) 683–692.
[47] O.S. Ahmad, T.S. Bedwell, C. Esen, A. Garcia-Cruz, S.A. Piletsky, Molecularly imprinted polymers in electrochemical and optical sensors, Trends. Biotechnol. 37 (2019) 294–309.
[48] Q.G. He, Y.L. Tian, Y.Y. Wu, J. Liu, G.L. Li, P.H. Deng, D.C. Chen, Facile and ultrasensitive determination of 4-nitrophenol based on acetylene black paste and graphene hybrid electrode, Nanomaterials 9 (2019) 429.
[49] R. Xing, S. Wang, Z. Bie, H. He, Z. Liu, Preparation of molecularly imprinted polymers specific to glycoproteins, glycans and monosaccharides via boronate affinity controllable–oriented surface imprinting, Nat. Protoc. 12 (5) (2017) 964–987.
[50] X. Zhang, S. Yang, R. Jiang, L. Sun, S. Pang, A. Luo, Fluorescent molecularly imprinted membranes as biosensor for the detection of target protein, Sens. Actuators, B 254 (2018) 1078–1086.
[51] B. Bali Prasad, A. Kumar, R. Singh, Synthesis of novel monomeric graphene quantum dots and corresponding nanocomposite with molecularly imprinted polymer for electrochemical detection of an anticancerous ifosfamide drug, Biosens. Bioelectron. 94 (2017) 1–9.
[52] F. Canfarotta, J. Czulak, A. Guerreiro, A.G. Cruz, S. Piletsky, G.E. Bergdahl, M. Hedström, B.o. Mattiasson, A novel capacitive sensor based on molecularly imprinted nanoparticles as recognition elements, Biosens. Bioelectron. 120 (2018) 108–114.
[53] Y.Y. Wu, P.H. Deng, Y.L. Tian, Z.Y. Ding, G.L. Li, J. Liu, Z. Zuberi, Q.G. He, Rapid recognition and determination of tryptophan by carbon nanotubes and molecularly imprinted polymer-modified glassy carbon electrode, Bioelectrochemistry 131 (2020) 107393.
[54] S. Khan, R. Chillawar, K. Tadi, R. Motghare, Molecular imprinted polymer based impedimetric sensor for trace level determination of digoxin in biological and pharmaceutical samples, Curr. Anal. Chem. 13 (2017) 474–482.
[55] Y. Yoshimi, Y. Yagisawa, R. Yamaguchi, M. Seki, Blood heparin sensor made from a paste electrode of graphite particles grafted with molecularly imprinted polymer, Sens. Actuators, B 259 (2018) 455–462.
[56] A.X. Liang, B. Tang, H.P. Hou, L.Q. Sun, A.Q. Luo, A novel $CuFe_2O_4$ nanospheres molecularly imprinted polymers modified electrochemical sensor for lysozyme determination, J. Electroanal. Chem. 853 (2019) 113465.
[57] J. Ju, R. Zhang, S. He, W. Chen, Nitrogen-doped graphene quantum dots-based fluorescent probe for the sensitive turn-on detection of glutathione and its cellular imaging, RSC Adv. 4 (94) (2014) 52583–52589.
[58] Y.-J. Yan, X.-W. He, W.-Y. Li, Y.-K. Zhang, Nitrogen-doped graphene quantum dots-labeled epitope imprinted polymer with double templates via the metal chelation for specific recognition of cytochrome c, Biosens. Bioelectron. 91 (2017) 253–261.
[59] D. Qu, M. Zheng, P. Du, Y. Zhou, L. Zhang, D. Li, Highly luminescent SN co-doped graphene quantum dots with broad visible absorption bands for visible light photocatalysts, Nanoscale 5 (2013) 12272.
[60] K. Chang, W.X. Chen, L-cysteine-assisted synthesis of layered MoS_2/graphene composites with excellent electrochemical performances for lithium ion batteries, ACS Nano 5 (2011) 4720–4728.
[61] S.K. Park, S.H. Yu, S. Woo, J. Ha, J. Shin, Y.E. Sung, A facile and green strategy for the synthesis of MoS_2 nanospheres with excellent Li-ion storage properties, CrystEngComm 14 (2012) 8323.
[62] Y. Guo, L. Zhang, X. Liu, B. Li, D. Tang, W. Liu, Synthesis of magnetic core-shell carbon dots@MFe_2O_4 (M = Mn, Zn and Cu) hybrid materials and their catalytic properties, J. Mater. Chem. A 4 (2016) 4044–4055.
[63] Y. Dong, J. Shao, C. Chen, H. Li, R. Wang, Y. Chi, X. Lin, G. Chen, Blue luminescent graphene quantum dots and graphene oxide prepared by tuning the carbonization degree of citric acid, Carbon 50 (2012) 4738–4743.
[64] J. Peng, W. Gao, B.K. Gupta, Z. Liu, R. Romero-Aburto, L. Ge, Graphene quantum dots derived from carbon fibers, Nano. Lett. 12 (2012) 844–849.
[65] L. Lin, X. Song, Y. Chen, M. Rong, T. Zhao, Y. Jiang, Y. Wang, X.i. Chen, One-pot synthesis of highly greenish-yellow fluorescent nitrogen-doped graphene quantum dots for pyrophosphate sensing via competitive coordination with Eu 3+ ions, Nanoscale 7 (2015) 15427–15433.
[66] L.M. Gassa, J.R. Vilche, M. Ebert, K. Jüttner, W.J. Lorenz, Electrochemical impedance spectroscopy on porous electrodes, J. Appl. Electrochem. 20 (1990) 677–685.

[67] S.K. Dhoke, A.S. Khanna, Electrochemical impedance spectroscopy (EIS) study of nano-alumina modified alkyd based waterborne coatings, Prog. Org. Coat. 74 (2012) 92–99.
[68] E. Casero, A.M. Parra-Alfambra, M.D. Petit-Domínguez, F. Pariente, E. Lorenzo, C. Alonso, Differentiation between graphene oxide and reduced graphene by electrochemical impedance spectroscopy (EIS), Electrochem. Commun. 20 (2012) 63–66.
[69] G. Liu, S.G. Iyengar, J.J. Gooding, An electrochemical impedance immunosensor based on gold nanoparticle-modified electrodes for the detection of HbA1c in human blood, Electroanalysis 24 (7) (2012) 1509–1516.
[70] J. Yang, T. Yang, Y. Feng, K. Jiao, A DNA electrochemical sensor based on nanogold-modified poly-2,6-pyridinedicarboxylic acid film and detection of PAT gene fragment, Anal. Biochem. 365 (2007) 24–30.
[71] B. Deiminiat, G.H. Rounaghi, Fabrication of a new electrochemical imprinted sensor for determination of ketamine based on modified polytyramine/sol-gel/f-MWCNTs@AuNPs nanocomposite/pencil graphite electrode, Sens. Actuators, B 259 (2018) 133–141.
[72] P.S. Sharma, A. Garcia-Cruz, M. Cieplak, K.R. Noworyta, W. Kutner, 'Gate effect' in molecularly imprinted polymers: the current state of understanding, Curr. Opin. Electrochem. 16 (2019) 50–56.
[73] Z. Wang, Y. Yang, J. Li, Organic–inorganic matrix for electrochemical immunoassay: detection of human IgG based on ZnO/chitosan composite, Talanta 69 (2006) 686–690.
[74] X. Zhang, G. Shen, S. Sun, Y. Shen, C. Zhang, A. Xiao, Direct immobilization of antibodies on dialdehyde cellulose film for convenient construction of an electrochemical immunosensor, Sensor. Actuat. B-Chem. 200 (2014) 304–309.
[75] H. Qi, C. Wang, N. Cheng, Label-free electrochemical impedance spectroscopy biosensor for the determination of human immunoglobulin G, Microchim. Acta 170 (2010) 33–38.
[76] Y. Liu, Y. Liu, H. Feng, Y. Wu, L. Joshi, X. Zeng, J. Li, Layer-by-layer assembly of chemical reduced graphene and carbon nanotubes for sensitive electrochemical immunoassay, Biosens. Bioelectron. 35 (2012) 63–68.
[77] P. Lach, P.S. Sharma, K. Golebiewska, M. Cieplak, F. D"Souza, W. Kutner, Molecularly imprinted polymer chemosensor for selective determination of an n-nitroso-l-proline food toxin, Chem-Eur J. 23 (8) (2017) 1942–1949.
[78] D. Zembrzuska, J. Kalecki, M. Cieplak, W. Lisowski, P. Borowicz, K. Noworyta, P. S. Sharma, Electrochemically initiated co-polymerization of monomers of different oxidation potentials for molecular imprinting of electroactive analyte, Sensor. Actuat. B-Chem. 298 (2019) 126884.